

## HiSST: 4th International Conference on High-Speed Vehicle Science Technology 22 -26 September 2025, Tours, France



# Total Temperature Measurements in High-speed Flows with Fiber Bragg Grating Sensors

Ignacio Lasala<sup>1</sup>, Avidh S. Bavkar<sup>1</sup>, Eric Bach<sup>1</sup>, Guillermo Paniagua<sup>1</sup>, Etienne Choquet<sup>2</sup>, Thierry Andre<sup>2</sup>

#### **Abstract**

Accurate total temperature measurements in high-speed flows are challenging due to unsteady probe—shock interactions, sensor-specific response characteristics, and errors arising from conduction, convection, radiation, and non-isentropic flow deceleration around the sensing element. While these error sources have been recognized and studied in the literature, most correction strategies treat them as independent, an assumption that breaks down in high-speed, high-temperature environments. Moreover, different total temperature probe designs exhibit varying sensitivities to these errors due to their distinct thermal and dynamic characteristics. This work assesses the accuracy of Fiber Bragg Grating (FBG) sensors relative to a conventional thermocouple probe in high-speed flow. It evaluates, compares, and proposes correction methods for velocity and conduction errors in both probe types.

This study evaluates temperature errors in an FBG temperature sensor housed in a Kiel shroud in sub- and supersonic jets at ambient and elevated temperatures. This is carried out side by side to a conventional thermocouple sensor enabling the comparison of both measurement technologies. The tests were conducted in the Facility for Instrumentation and Open jet Research (FIOR) of PETAL, which is a converging nozzle of 80 mm exhaust diameter, and seek to compare the velocity error and conduction error of both types of probes, as well as to develop and evaluate a common correction methodology. Each dynamic test consisted of a temperature stabilization period of 15 minutes at Mach 0.45, and several stable blowdowns at Mach numbers ranging from 0.3 to 1.1 at both room temperature and heated conditions (100°C). The tests were coupled with IR videos that recorded the temperature at the probe support. The data from all tests were used to fit the temperature response to a combined velocity—conduction error model. This approach helps quantify the contribution of each error source to the sensor's response and enables the retrieval of the true total temperature. The model requires as inputs the Mach number, the sensor reading, and the probe support temperature obtained from infrared measurements. Overall, this study provides a strong foundation for improving temperature measurement accuracy in high-speed flows and offers valuable insight into the performance of both FBG sensors and thermocouples for aerospace applications.

**Keywords**: total temperature measurement, fiber Bragg grating, conduction error correction, velocity error correction, high-speed flows

#### **Nomenclature**

Latin

B – Bias uncertainty

Cp – Specific heat

d – Diameter

h – Heat transfer coefficient

k – Thermal conductivity

L – Length

N – Number of samples

n – refractive index

P - Perimeter

q – Heat flux

S – Sample standard deviation

T – Temperature

V - Velocity (or) Voltage

HiSST-2025-278
Total Temperature Measurements in High-speed Flows with Fiber Gragg Grating Sensors

<sup>&</sup>lt;sup>1</sup> Maurice J. Zucrow Laboratories, Purdue University, West Lafayette, IN, USA

<sup>&</sup>lt;sup>2</sup> MBDA, Le Plessis Robinson, France

z – Thickness

Greek

 $\Delta$  – Overall uncertainty

 $\lambda$  – Wavelength

 $\nu$  – Viscosity

 $\sigma$  – Stochastic uncertainty

 $\phi$  – Fit coefficient

Dimensionless groups

M – Mach number

Nu – Nusselt number

Re – Reynolds number

r – recovery factor

Subscripts

0 - Total conditions

 $\infty$  – Free stream conditions

a – Air

ad – Adiabatic conditions

c - Critical conditions

jc – Thermocouple junction

cjc – Thermocouple cold junction

sn - Sensor

sp – Probe casing/support

 $sp_{\rm int}$  – Internal wall of probe casing

 $sp_{\rm ext}$  – External wall of probe casing

w – Wire

#### 1. Introduction

Accurate total temperature measurements are of paramount importance across a wide range of fundamental and applied configurations in fluid dynamics, extending to high velocity environments. Non-intrusive optical techniques offer the benefit of minimizing flow disturbance, but at the same time require complex calibrations and a high degree of optical access. Temperature sensing with flow probes thus remains a highly utilized [1] and well-established [2] method, commonly making use of a vented Kiel type probe housing a thermocouple sensor [3]. The temperature reading obtained by the combination of probe and sensing element diverges from the actual total temperature of the flow due to different modes of heat transfer and incomplete conversion of kinetic to thermal energy, requiring an a posteriori correction [4]. Correction factors specific to a given probe and sensor combination need to be determined in a separate experiment with well-defined boundary conditions to reduce uncertainty; however, determining the boundary conditions for the interacting heat transfer phenomena present considerable challenges that affect the reliability of the correction factors obtained. Additionally, while the correction factor formulations are not probe-specific, their application has been predominantly limited to thermocouple probes.

In the field of diagnostics with flow probes, a promising alternative to traditional thermocouples are sensors based on distributed Bragg reflectors inscribed into optical fibers, so-called fiber Bragg gratings (FBG). They constitute a periodic perturbation of the refractive index along the fiber length, resulting in a wavelength-specific dielectric mirror. Since their first demonstration in the late 1970s, FBGs have matured into commercial products [5]. When illuminated with a broadband light source, only a narrowband component is reflected at the Bragg wavelength. Perturbation of the grating results in a shift of this Bragg wavelength, which can in turn be detected in the reflected spectrum. A perturbation can be induced due to mechanical strain or temperature changes. In temperature probes, the dependence of Bragg wavelength on temperature arises due to variations in the index of refraction of the glass and the thermal expansion of the grating. In silica fibers, the former of these is the dominant effect, accounting for roughly 95% of the observed shift [6].

As the Bragg wavelength of a given grating can be finely controlled during the production process, multiple gratings with different properties can be arranged along a single fiber, creating a chain of inline sensors. Illumination with a single light source and detection of the reflected spectrum allows monitoring of the temperature and strain at several fiber gratings with a single optical interrogator. This approach has been developed into a number of commercial off-the-shelf components, and research efforts are ongoing to expand the application range to higher temperatures, higher grating density, and derived physical quantities such as acceleration or pressure sensing [7]. FBGs in silica fibers can be annealed and regenerated to allow for stability at higher temperatures, or the gratings can be inscribed by femtosecond lasers to achieve a similar effect [8], [9]. Beyond that, sapphire fibers may be used, although these are inherently multimode [10], [11]. Advancements were also made towards the packaging [12], [13], [14] and calibration [15], [16] of multi-point sensors on a single optical fiber for harsh, high-temperature and high-velocity [17], [18] or shock-laden [19], [20] environments. It is evident from these results that FBGs offer an attractive and highly capable packaging solution for multi-point, multi-resolution temperature sensing.

The present work addresses two key issues: (i) correcting sensor temperature measurements in high-

speed, heated flow conditions to more accurately approximate the stagnation temperature, and (ii) evaluating the performance of an off-the-shelf FBG sensor relative to a conventional thermocouple probe with respect to heat-transfer-related temperature errors. First, a fitting function is developed to separate conduction and velocity error contributions using accessible boundary conditions. Next, an experimental campaign is conducted in a calibration facility under varying Mach numbers and flow heating conditions to characterize these error sources. Finally, the performance of thermocouple and FBG sensors is compared, and their readings are corrected to recover the stagnation flow temperature with quantifiable uncertainties throughout the correction process. This combined methodology enables full experimental characterization of probe performance, correction of measurements to stagnation temperature, and quantification of the uncertainty introduced by the correction—applicable not only to thermocouples and FBG sensors but extendable to other temperature probes.

## 2. Velocity and Conduction Error in Total Temperature Probes

## 2.1. Review of Velocity and Conduction Error Models

The temperature of an intrusive sensor stabilizes when convective heat transfer from gas to sensor balances the heat flow by radiation and conduction. The presence of kinetic energy dissipation in the boundary layer, conduction to the support, or radiative flux, prevents the sensor from measuring the total temperature of the gas. These deviations from the ideal behavior are known as velocity, conduction, and radiation errors. Early models assumed these contributions are independent [21], [22], [23], however, this assumption fails in high-speed, high-temperature flows, where convection and velocity errors dominate and interact [24]. In the absence of radiation, Villafañe and Paniagua introduced a model that preserves the coupled nature of heat transfer mechanisms, while enabling separation of individual contributions via the adiabatic wall temperature as a linking term [25].

$$(1-Z) = \frac{T_0 - T_{sn}}{T_0 - T_{\infty}} = \frac{\tilde{T}_0 - T_{ad}}{T_0 - T_{\infty}} + \frac{\tilde{T}_{ad} - T_{sn}}{T_{ad} - T_{sp_{int}}} \frac{\tilde{T}_{ad} - T_{sp_{int}}}{T_0 - T_{\infty}}$$
(1)

Where Z is the overall recovery factor defined as the difference between the measured temperature and the total gas temperature, relative to the dynamic temperature. The first term (a) is the velocity error, and the second and third terms (b, c), are the conduction error that depends on the remaining heat transfer processes in the wire, shield, stem, and external probe support. This definition is primarily applied in CFD studies. Its experimental use is limited due to the difficulty of determining the adiabatic wall temperature in the absence of truly adiabatic boundaries. A schematic of the different errors defined in Equation (1) is shown in Figure 1 for a generic thermocouple junction.

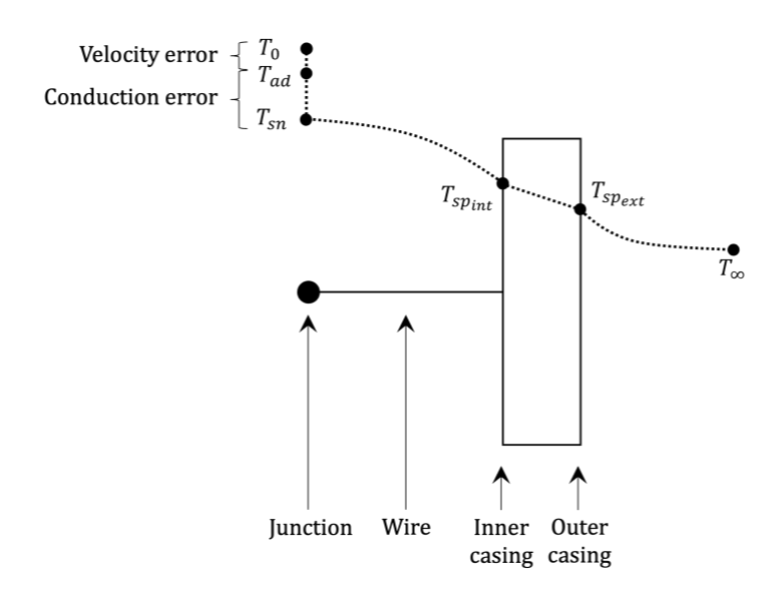


Figure 1: Temperature errors and temperature profile in a thermocouple probe.

The velocity error (a) is modeled using the recovery factor r, which represents the fraction of kinetic energy recovered at the junction and is defined in Equation (2). It depends on the geometry of the immersed body, flow angle, and the Prandtl number of the fluid. This error increases at high speeds, as already at Mach 1, kinetic energy represents 16.7% of the total energy of the gas [24]. The independent contributions assumption would replace  $T_0 - T_{ad}$  by  $T_0 - T_{sn}$ , but that would neglect any effect of other heat transfer mechanisms on the temperature error.

$$\frac{T_0 - T_{ad}}{T_0 - T_{\infty}} = 1 - \frac{T_0 - T_{ad}}{\frac{V_{\infty}^2}{2C_p}} = r$$
 (2)

Conduction errors can be estimated from the equations of heat transfer across a thin fin with adiabatic tip and isothermal casing. The solution for the wire temperature distribution is shown in Equation (3) [26]. As before, the independent contributions assumption would replace every  $T_{ad}$  by  $T_0$ , neglecting interactions between effects. This equation requires knowing the temperature of the internal casing, which is not trivial; If an additional sensor is used to measure it, it would be subject to the same errors that are trying to be corrected. Other strategies try to get rid of conduction error rather than modelling it. Strategies include heating the probe support to near flow temperature to prevent heat transfer [27]; or using dual-wire probe designs where both wires share a common support temperature, allowing it to cancel out through combined equations [28], [29].

$$\frac{T_{ad} - T_{sn}}{T_{ad} - T_{sp_{int}}} = \frac{1}{\cosh\left(L_w \sqrt{\frac{4h_w}{d_w k_w}}\right)} = \frac{1}{\cosh\left(\frac{L_w}{L_c}\right)}$$
(3)

Radiation errors are only significant at high flow temperatures. At the conditions of this study, there was a maximum difference of ±40 °C between the flow and shield temperature. Assuming the worst case - unit view factor and equal conductive and radiative areas [24] - the estimated radiation error was negligible, below  $10^{-3}$  %, and thus it will be neglected from now on.

## 2.2. Development of a Combined Fit Function for Velocity and Conduction Errors

A methodology is sought that decomposes the total error, as in Equation (1), into its conduction- and velocity-related components while preserving their coupled nature. The approach first establishes separate functional forms for the velocity and conduction errors, dependent on Mach and Reynolds numbers, respectively. To determine the coefficients of these functional forms, experiments must be conducted; therefore, the errors need to be retrieved in a way that avoids reliance on quantities that are either impractical to measure, such as the internal casing temperature, or not directly accessible under experimental conditions, such as the adiabatic wall temperature. To achieve this, the conduction error model is reformulated in terms of the external casing temperature, which can be measured using optical diagnostics such as infrared thermography. In parallel, the adiabatic wall temperature is algebraically eliminated, since it appears in both the velocity and conduction error models.

The resulting expression relates the true total temperature to measurable quantities—sensor temperature and external casing temperature—along with the coefficients of the fitted functional forms for each error, which will be discussed in the next subsection. An experimental campaign over a range of Mach numbers and flow heating conditions provides the database required to determine these coefficients consistently. Once identified, the formulation enables direct comparison of the sensitivity of the thermocouple and FBG probe to each error and facilitates stagnation temperature retrieval in facilities where the total temperature is not known a priori, thereby extending the method's applicability beyond the calibration environment. The methodology is summarized in Figure 2.

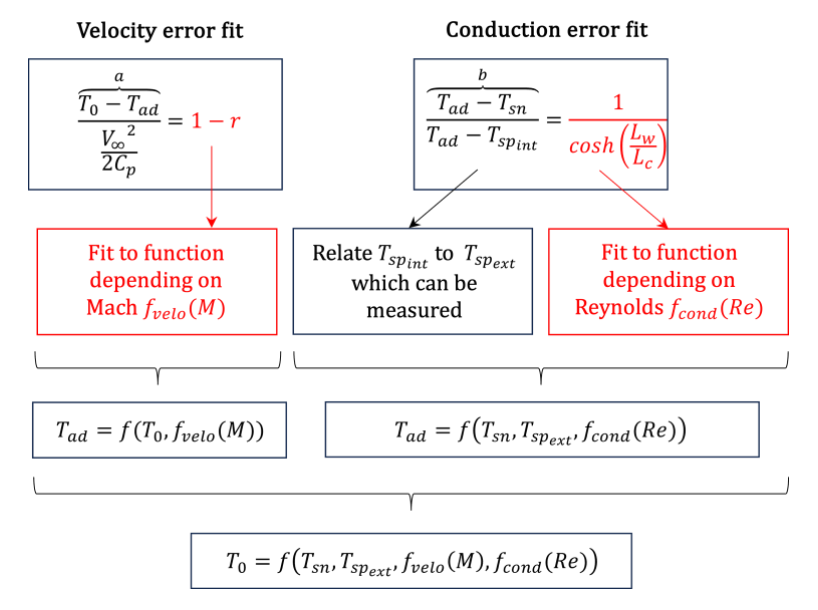


Figure 2: Process to obtain the fit function to correct for velocity and conduction effects.

The functional form to model the velocity error was presented by Sanchez and Paniagua [29] and is shown in Equation (4). It comes from a linear relation between the recovery ratio and the Mach number, that transforms into a rational fit of second order for the recovery factor. The original equation asymptotically tends to 1 ( $\phi_1 = 1$ ), but it has been relaxed to allow the asymptote to stabilize at lower recovery factors. Moffat summarized the recovery factors for different probes with wires perpendicular to the flow and reported an asymptotic value of 0.68 in unshielded probes and 0.95 in shielded designs [24], both smaller than 1.

$$r = \phi_1 + \frac{\phi_2}{M} + \frac{\phi_3}{M^2} \tag{4}$$

## 2.3. Functional Form of the Conduction Error Fit

Equation (3) requires knowledge of the temperature inside the casing, in the base of the wire. However, the heat transfer problem can be extended to model heat transfer across the casing and substitute the internal casing temperature by the external one, which can be monitored with nonintrusive techniques like infrared thermography.

The entire heat transfer to the casing is a combined effect of the one that occurs in the location of the wire (pure conduction) and the rest of the casing in direct contact with the air flow (convection). In order to account only for the conduction heat transfer from the wire, conduction across the shield will be considered using as cross section the one of the wires instead of the entire surface area of the shield. Equation (5) is the conductive heat flux across the casing and Equation (6) is the heat flux at the base of the wire from the fin approximation [26]. When equated, they result in Equation (7).

$$q_{shield} = -k_{sp}A_w \frac{T_{sp_{int}} - T_{sp_{ext}}}{z} \tag{5}$$

$$q_{base} = \sqrt{hP_w k_w A_w} \cdot \left(T_{sp_{int}} - T_{ad}\right) \cdot tanh\left(\frac{L_w}{L_c}\right) \tag{6}$$

$$T_{sp_{int}} - T_{sp_{ext}} = -\underbrace{\frac{z}{k_{sp}A_w} \sqrt{hP_w k_w A_w} \cdot tanh\left(\frac{L_w}{L_c}\right)}_{\chi} \left(T_{sp_{int}} - T_{ad}\right) \tag{7}$$

Parameter  $\chi$ , which modulates both temperature differences in Equation (7) depends on geometrical characteristics and the convective heat transfer coefficient h. This relation allows to isolate  $T_{sp_{int}}$  as shown in Equation (8).

HiSST-2025-278 Page | 5
Total Temperature Measurements in High-speed Flows with Fiber Gragg Grating Sensors Copyright © 2025 by author(s)

$$T_{sp_{int}} = \frac{T_{sp_{ext}} + \chi T_{ad}}{1 + \chi} \tag{8}$$

Only if the shield is sufficiently thin, with high conductivity, or the heat transfer coefficient in the wire is small,  $\chi$  will tend to 0 and the temperature at both sides of the shield will be almost the same  $T_{sp_{int}} \approx$  $T_{sp_{ext}}$ . Otherwise, this difference has to be accounted.

Equation (9) shows the modified equation depending on the outer casing temperature, which only differs from Equation (3) by the new factor in the denominator  $(1 + \chi)$ . Both  $\chi$  and  $L_c$  are factors whose only variable is the heat transfer coefficient for a given probe geometry. Equation (9) can be expanded into Equation (10) to explicitly show this dependence.

$$T_{ad} - T_{sn} = \frac{T_{ad} - \frac{T_{sp_{ext}} + \chi T_{ad}}{1 + \chi}}{\cosh\left(\frac{L}{L_c}\right)} = \frac{T_{ad} - T_{sp_{ext}}}{(1 + \chi) \cdot \cosh\left(\frac{L}{L_c}\right)}$$
(9)

$$T_{ad} - T_{sn} = \frac{T_{ad} - \frac{T_{sp_{ext}} + \chi T_{ad}}{1 + \chi}}{\cosh\left(\frac{L}{L_c}\right)} = \frac{T_{ad} - T_{sp_{ext}}}{(1 + \chi) \cdot \cosh\left(\frac{L}{L_c}\right)}$$

$$\frac{T_{ad} - T_{sn}}{T_{ad} - T_{sp_{ext}}} = \frac{1}{\left(1 + \frac{z \, k_w}{k_{sp}} \sqrt{\frac{P_w}{k_w A_w}} \sqrt{h} \cdot \tanh\left(\sqrt{\frac{P_w}{k_w A_w}} L_w \sqrt{h}\right)\right) \cdot \cosh\left(\sqrt{\frac{P_w}{k_w A_w}} L_w \sqrt{h}\right)}$$

$$(10)$$

The heat transfer coefficient in the wires can be modelled using Equation (11) for wires perpendicular to the flow as recommended by Moffat [24], using total gas properties to evaluate the Reynolds and Nusselt number as recommended by Seadron and Warshawsky [30]. A Prandtl number correction is omitted but would be needed to use this approach for different gases.

$$\bar{h} = \frac{k_a}{d_w} Nu = \frac{k_a}{d_w} (0.44 \pm 0.06) \cdot Re_D^{0.5}$$
(11)

$$Re_D = \frac{d_w V}{v_0} \tag{12}$$

Equation (13) shows the result of introducing the heat transfer coefficient correlation into Equation (10). The common constant coefficients have been grouped into the term  $\phi_4$  that will be found experimentally. Although  $\phi_4$  has an analytical definition shown in Equation (14), this conduction model is a simplification of the real behavior, so  $\phi_4$  will be found through an experimental calibration to better model the behavior of each specific probe.

$$\frac{T_{ad} - T_{sn}}{T_{ad} - T_{sp_{ext}}} = \frac{1}{\left(1 + \frac{z \, k_w}{k_{SD}} \, \phi_4 Re_D^{\frac{0.5}{2}} \cdot tanh\left(L_w \, \phi_4 Re_D^{\frac{0.5}{2}}\right)\right) \cdot cosh\left(L_w \, \phi_4 Re_D^{\frac{0.5}{2}}\right)} \tag{13}$$

$$\phi_4 = \sqrt{\frac{(0.44 \pm 0.06) P_w k_a}{A_w k_w d_w}} \tag{14}$$

In the end, the velocity error model depends only on Mach number (Equation 15), and the conduction error model depends only on Reynolds number and geometric coefficients (Equation 16). Both equations can be combined following the process shown in Figure 2, resulting in Equation 17. This allows the total temperature of the flow to be calculated from the sensor temperature, the external support temperature, and the freestream Mach and Reynolds numbers, once the fit coefficients are obtained from an ad-hoc experimental calibration.

$$f_{velo}(\phi_1, \phi_2, \phi_3, M) = \phi_1 + \frac{\phi_2}{M} + \frac{\phi_3}{M^2}$$
 (15)

$$f_{cond}(\phi_4, Re) = \left(1 + \frac{z k_w}{k_{sp}} \phi_4 Re_D^{\frac{0.5}{2}} \cdot tanh\left(L_w \phi_4 Re_D^{\frac{0.5}{2}}\right)\right) \cdot cosh\left(L_w \phi_4 Re_D^{\frac{0.5}{2}}\right)$$
(16)

$$T_{0} = \frac{1}{f_{cond}(\phi_{4}, Re)} \left[ f_{cond}(\phi_{4}, Re) \cdot T_{sn} - T_{sp_{ext}} \right] + \left( 1 - f_{velo}(\phi_{1}, \phi_{2}, \phi_{3}M) \right) \frac{V^{2}}{2C_{p}}$$

$$(17)$$

## 3. Testing Facility

#### 3.1. Open Jet Test Rig

The tests presented in this article were conducted at the Purdue Experimental Turbine Aerothermal Lab (PETAL) [31] using the Facility for Instrumentation and Open Jet Research (FIOR) fed by the pressure-driven wind tunnel Petal Tunnel 1 (PT1).

PT1 is a long-duration, pressure-driven wind tunnel capable of operating over a wide range of Reynolds and Mach numbers. It is fed by a 56 m³ dry air reservoir pressurized to 150 bar, discharging to ambient when the open test section (FIOR) is installed, or alternatively into a 283 m³ vacuum tank maintained at 10 mbar. The air supply passes through a natural gas-fired heat exchanger, delivering non-vitiated air at up to 600 K. Mass flow is measured with a calibrated venturi and purged until a fast-actuating butterfly valve initiates flow through the tunnel. A settling chamber with honeycomb and mesh screens homogenizes the flow before it reaches FIOR. At maximum mass flow conditions, the velocity in the settling chamber reaches Mach 0.035, preserving 99.91% of total pressure.

FIOR is a converging nozzle designed to deliver uniform, homogeneous flow at various Mach numbers and temperatures. It features an 80 mm exhaust diameter to allow the calibration of large probes with minimal blockage or shear layer ingestion. The internal surface is shaped without inflection points to promote a thin boundary layer along the nozzle wall. The schematic of PT1 with the FIOR test section installed is shown in Figure 3.

A variety of instruments are installed along the wind tunnel and test section to accurately characterize the flow. Up to six Type-K thermocouples (K1X-S304-062-EX-12-MPCX, Evolution Sensors and Controls, LLC) were used upstream of the nozzle for reference temperature measurements. These sensors were calibrated following the static calibration procedure explained in later sections. Temperature data is acquired using a 48-Channel precision thermocouple measurement instrument (EX1048, VTI Instruments), with every four channels featuring an independent cold junction measured by an RTD. Pressure measurements were taken using a pressure scanner (Scanivalve MPS4264) module, which recorded data from two total pressure ports in the settling chamber and 25 static pressure ports along the nozzle wall. The module has an accuracy of 0.0621 kPa.

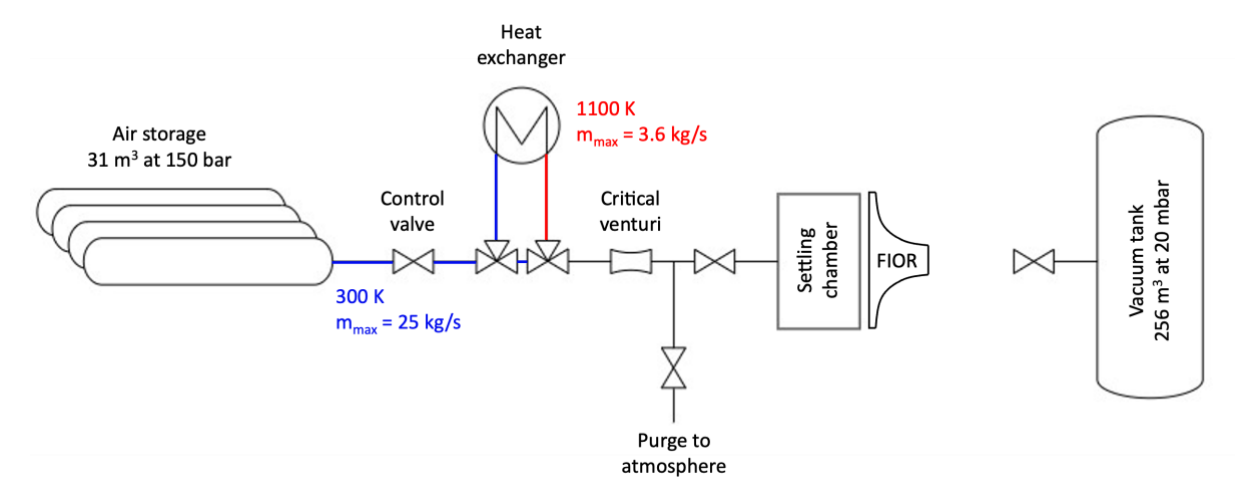


Figure 3. PT1 wind tunnel schematic with the FIOR test section.

#### 3.2. Test Setup and Instrumentation

Two identical probe mounts were designed to house the thermocouple and the FBG sensor, ensuring that the influence of stem geometry was eliminated in the comparison of their performance. Each mount featured a protective shield with an internal diameter of 3.89 mm and a length-to-diameter (L/D) ratio of 3. The thickness of the Kiel shield was 0.81 mm. A single bleed hole was positioned at the rear of the probe, resulting in an inlet-to-bleed area ratio of 4 [32]. Both probe mounts were 3D printed in polyether ether ketone (PEEK), as it maintains its stiffness up to elevated temperatures allowing continuous testing at more than 100 °C.

The thermocouple used for calibration was a Type K, fast-response model with an exposed junction (K1X-S304-062-EX-12-MPCX, Evolution Sensors and Controls, LLC). It was inserted through the bottom of the probe stem until the tip of the stainless-steel sheath was flush with the inside of the Kiel shield, and the junction close to the middle. The thermocouple signal was acquired using the EX1048 system from VTI Instruments sampled at 800 Hz.

The FBG sensor was a dielectric temperature probe (FS63DTP, Hottinger Brüel & Kjær Inc.) with a center Bragg wavelength of 1575 nm, and a specified operating range of -40 °C to 200 °C. Interrogation was performed using an optical interrogation unit (QuantumX MSFS BraggMETER - 1-MXFS8DI1/FC, Hottinger Brüel & Kjær Inc.), capable of reading up to 8 independent fibers with a maximum of 16 gratings per fiber. The FBG signal was sampled at 1 kHz.

Both probes were secured downstream of the nozzle using a KUKA KR 6 R700 six-axis robotic arm. The two probe heads were installed symmetrically about the nozzle centerline, with a distance between heads of 4 cm. The detailed geometry of the probe mounts and the relative positioning of the sensing elements with respect to the Kiel shield are shown in the close-up view in Figure 4.

The external surface temperature of the Kiel shield was monitored using an infrared camera (FAST-V1K, Telops Inc.) operating at an acquisition rate of 50 Hz and an exposure time of 45 µs. These settings were selected to achieve approximately 80% pixel well-filling at 370 K, maximizing dynamic range while avoiding saturation across all temperature conditions encountered during testing. The IR diagnostics were calibrated following an in-situ methodology that is explained in later sections. Figure 4 provides a schematic of the test setup, showing the location and integration of the infrared diagnostics, and the probe calibration configuration.

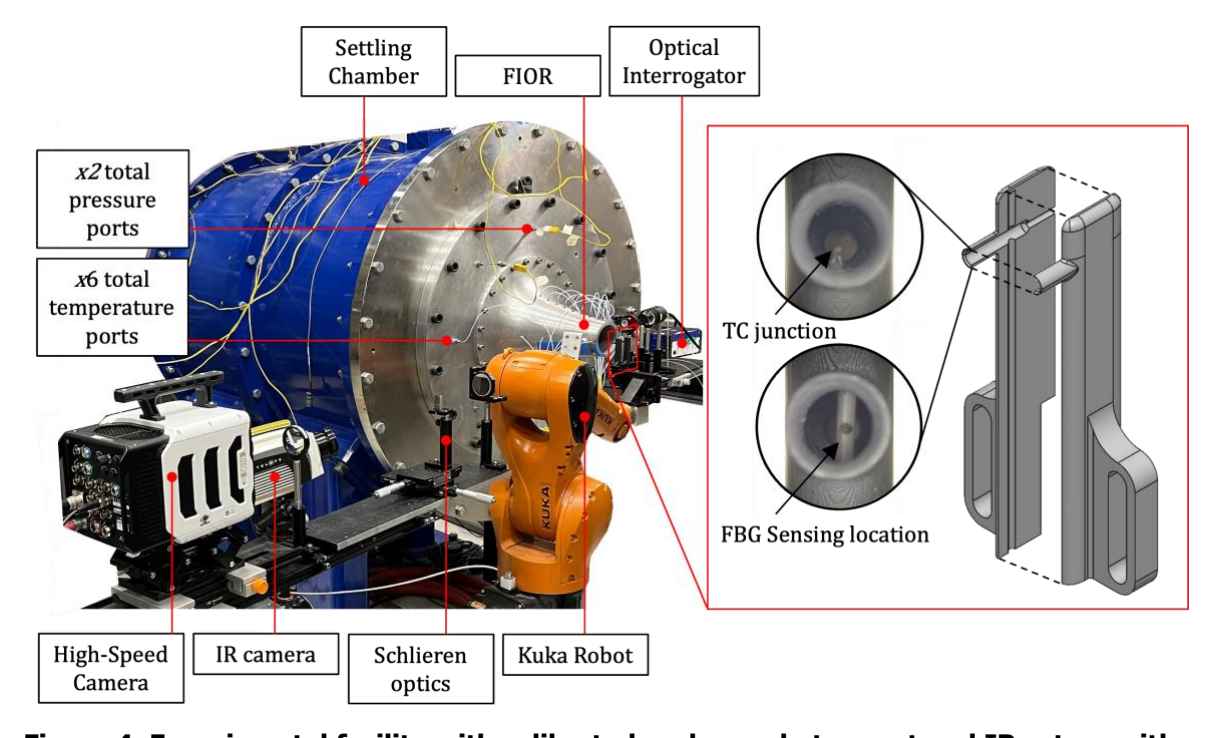


Figure 4. Experimental facility with calibrated probes, robot mount and IR setup; with a close-up view of the calibrated probes and the geometry of the sensing location within the Kiel shield.

HiSST-2025-278 Page | 8 Ignacio Lasala, Avidh S. Bavkar, Eric Bach, Guillermo Paniagua, Etienne Choquet, Thierry Andre Copyright © 2025 by author(s)

## 4. Calibration Methodology

#### 4.1. Static Calibration

The static calibration is the first step to get rid of all environment-related errors and create the best fit between temperature at the sensing and the magnitude measured (voltage for the thermocouple, and wavelength shift for the FBG). The static calibration has been followed according to the NIST Special Publication 250-35 [33] and the VDI/VDE 2660 Blatt 2:2020-04 [34] standard for Thermocouple and FBG probes calibration respectively.

Every thermocouple and FBG sensor used in the present work has been calibrated to obtain individual calibration coefficients. The same data acquisition system, channel, and settings used during testing are used during this calibration to include the environmental conditions from the facility in the calculated coefficients. Uncertainty analysis is also performed on the calibration coefficients. A 9170 metrology well from FLUKE is used for the calibration. This device maintains temperature setpoints in a  $\pm 0.005$  K range. Calibrations were made for eight setpoints and were ran several times for every sensor.

## 4.1.1. Calibration Equations

Thermocouples provide a specific voltage depending on the temperature difference between the junctions. This relation is linear for the range of operation of the thermocouple used. The junction temperature can be retrieved using Equation (18), where  $T_{jc}$  and  $T_{cjc}$  are the junction and cold junction compensation temperatures, and  $a_i$  are the fit coefficients.

$$T_{ic} - T_{cic} = a_0 \cdot V + a_1 \tag{18}$$

For a single mode FBG sensor (zero-order FBG) the wavelength of the reflected beam is dependent on the grating period and the refractive index of the fiber, both of which are affected by strain and temperature as shown in Equation (19). For a temperature sensor (subjected to 0 axial strain), all the variations in the grating length and refractive index are due to temperature. In practice, the change in wavelength is approximated to a linear relationship with temperature modulated by the thermal expansion ( $\alpha$ ) and the thermo-optical ( $\xi$ ) coefficient shown in Equation (20). However, the modulating coefficients also depend on temperature in a non-linear manner, so the use of a linear fit to calibrate the FBG behavior is constrained to a small temperature range. In practice, higher order polynomials are used [34]. The temperature range of this study spans  $\pm 150K$ , and a third-order polynomial is recommended [34], shown in Equation (21).

$$\lambda_B = 2\frac{\Lambda}{k} n_{eff} \tag{19}$$

$$\frac{\Delta \lambda_B}{\lambda_R} \approx (\alpha + \xi) \Delta T \tag{20}$$

$$T_{FBG} = b_0 + b_1 \cdot (\lambda - \lambda_0) + b_2 \cdot (\lambda - \lambda_0)^2 + b_3 \cdot (\lambda - \lambda_0)^3$$
 (21)

#### 4.1.2. Uncertainty in Static Calibration

The 95% confidence intervals for the calibration coefficients of a n-order polynomial fit can be obtained via the least squares method as the square roots of the diagonal elements of the covariance matrix. This procedure is automatically implemented in MATLAB through the fitlm function. Each coefficient will provide an individual systematic error or bias that can be grouped to find the overall bias uncertainty B. The measured properties have a bias contribution due to errors in the measurement instruments, but also stochastic contributions due to noise and the randomness of the data  $\sigma$ . Both contributions have to be accounted for in order to compute the overall uncertainty  $\Delta$ , all shown in Equation (22). Equations (23) and (24) show the bias and stochastic uncertainty formulas for the thermocouple and Equations (25) and (26) for the FBG, where the wavelength shift is rewritten as  $\lambda_s =$  $(\lambda - \lambda_0)$ .

$$B = \sqrt{\left(\frac{\partial T}{\partial x}B_x\right)^2 + \left(\frac{\partial T}{\partial y}B_y\right)^2 + \cdots}, \qquad \sigma = \sqrt{\left(\frac{\partial T}{\partial z}\frac{S_z}{\sqrt{N-1}}\right)^2 + \cdots}, \qquad \Delta = t_{0.95}\sqrt{B^2 + \sigma^2}$$
 (22)

$$B_{T_{TC}} = \sqrt{\left(V B_{a_0}\right)^2 + \left(B_{b_0}\right)^2 + \left(B_{T_{cjc}}\right)^2 + (a_0 B_V)^2}$$
 (23)

$$\sigma_{T_{TC}} = \sqrt{\left(a_0 \frac{S_V}{\sqrt{N-1}}\right)^2 + \left(\frac{S_{T_{cjc}}}{\sqrt{N-1}}\right)^2}$$
 (24)

$$B_{T_{FBG}} = \sqrt{(B_{b_0})^2 + (\lambda_s B_{b_1})^2 + (\lambda_s^2 B_{b_2})^2 + (\lambda_s^3 B_{b_3})^2 + ((3b_3 \lambda_s^2 + 2b_2 \lambda_s + b_1) B_{\lambda_s})^2}$$
 (25)

$$\sigma_{T_{FBG}} = \sqrt{\left(\left(3b_3\lambda_s^2 + 2b_2\lambda_s + b_1\right)\frac{S_{\lambda_s}}{\sqrt{N-1}}\right)^2} \tag{26}$$

This allows to retrieve the respective fits with uncertainty bands, as shown in Figure 5. Although the nonlinearity in the FBG data is small, fitting a linear function to the data would increase the overall error by an order of magnitude in the calibrated range. A small nonlinearity can also be seen in the thermocouple data, but even with it, the maximum error is within  $\pm 0.5 K$ .

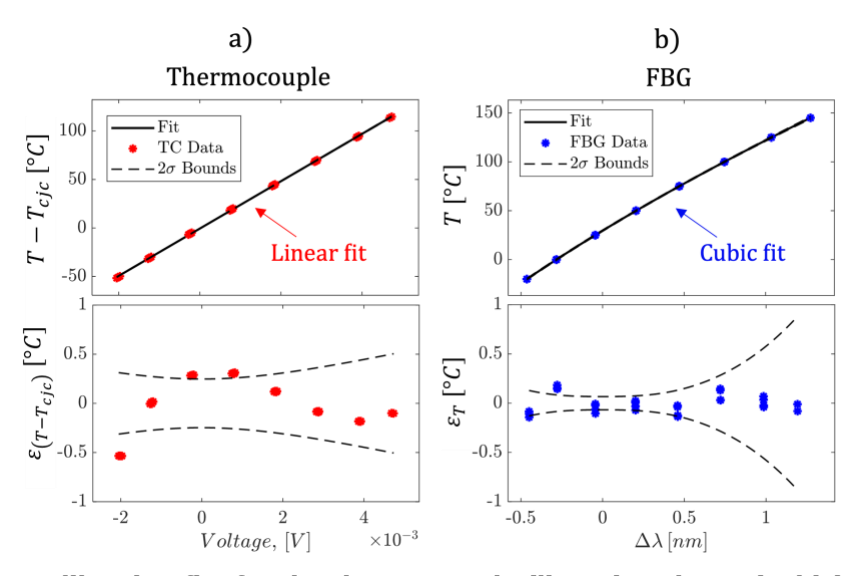


Figure 5. Calibration fits for the thermocouple (linear) and FBG (cubic) with their associated 95% confidence intervals based on the standard error of least square method

#### 4.2. Velocity and Conduction Error Calibration

## 4.2.1. Test Setup, Sequence and Conditions

Two calibration runs were performed: one with unheated flow at  $\sim\!270\,\text{K}$ , and one with heated flow at  $\sim\!370\,\text{K}$ . In the first run, air from high-pressure tanks was injected directly into the test section. The Mach number was ramped from 0.3 to 1.1 and back down in two full cycles, in steps of about  $\pm0.15$ . In the second run, part of the airflow passed through a natural gas heat exchanger to increase the total temperature, and the Mach number cycle was repeated. During the test, the Mach number and total temperature are derived from the 6 total temperature and 2 total pressure sensors inside the settling chamber, and the static (ambient) pressure is measured with a Druck DPI612 calibrator with an uncertainty below 0.1 mbar. The readings from the thermocouple and FBG probes are sampled continuously throughout hour-long tests. The infrared measurements of the stem temperature are triggered at specific times once the temperature stabilizes after a flow rate setpoint is changed.

Figure 6 shows a representative example of the calibration. In Figure 6a, the Mach number trace shows the two full cycles completed during the unheated run. In the heated run, only one ramp-up was possible due to limited air storage. Figure 6b compares the total temperature in the settling chamber with readings from the thermocouple and FBG probes. All three signals show similar trends, but with deviations showcasing the existence of the explained temperature errors. A reference thermocouple was adhered to the wall of the nozzle to calibrate the IR system by comparing raw IR signals to actual wall temperatures. After calibration, the IR readings (black squares) replicate the trend of the thermocouple (grey line). Once calibrated, the IR camera was used to measure the probe stem temperature from the same video frames (red squares). Finally, Figure 6c shows the combined temperature error for both probes. Two key trends are visible. First, the error increases with Mach number, consistent with velocity-induced effects. Second, the error is higher in the heated case as the temperature difference between the flow and the stem is higher, consistent with conduction-induced effects. The FBG probe consistently shows larger errors than the thermocouple, even though both follow the same trend.

These results show that total temperature errors of up to 5 K can occur even in a simple, steady, open-jet setup operating just 100 K above ambient at transonic speeds. This highlights the need to correct for both conduction and velocity-related error sources in temperature measurements.

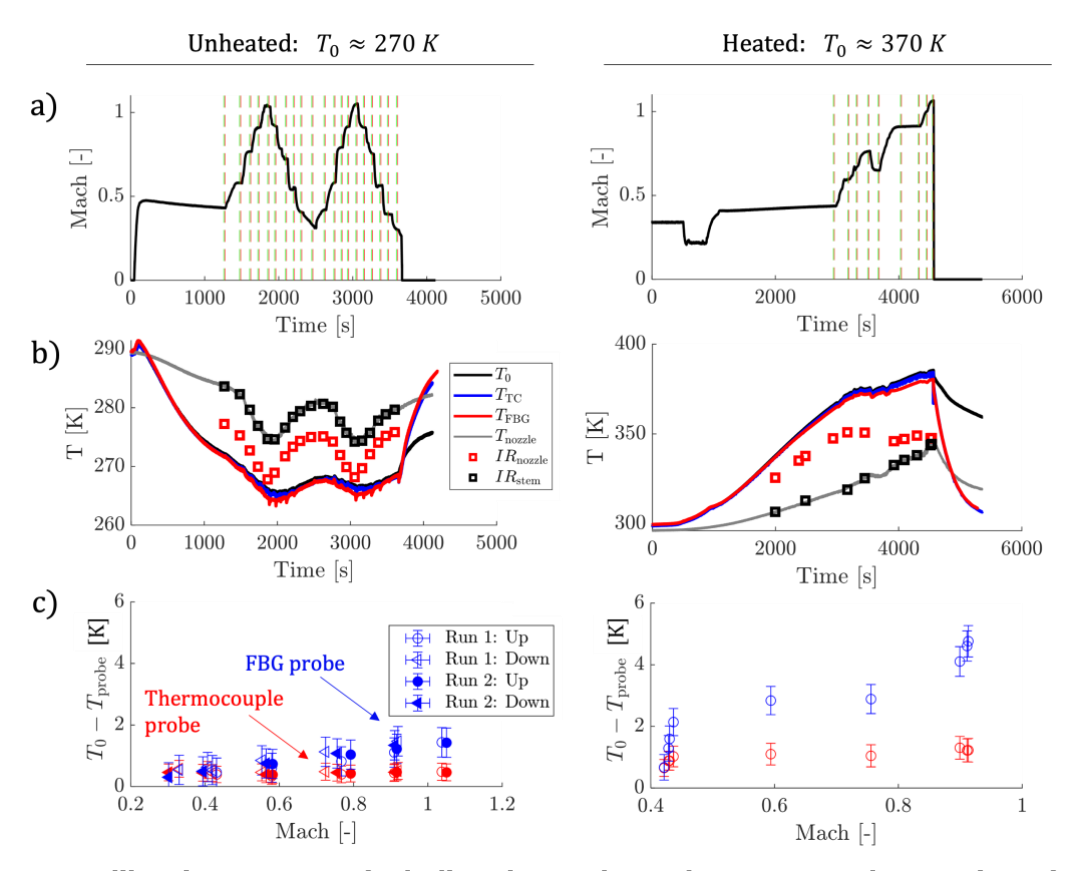


Figure 6. Calibration summary including the Mach number traces and averaging windows (a) the flow and surface temperature traces from thermocouples, FBG and IR (b), and the overall temperature errors for both probes in unheated and heated conditions (c).

## 4.2.2. Infrared Thermography Calibration and Data Collection

Infrared thermography measurements are calibrated following the in-situ calibration procedure outlined by Ostrowski and Schiffer [35]. IR measurements are directly compared to surface thermocouple readings during the test to find calibration coefficients and avoid additional corrections due to environmental effects.

Attaching surface thermocouples to the test article is challenging, so the reference thermocouple is placed in the external wall of the nozzle, which is also included in the field of view of the camera shown

in Figure 7, but is not exposed to flow. If the nozzle and the probe stem are ensured to have the same emissivity, and similar viewing angle, the same calibration coefficients can be applied for both as the environmental conditions are the same. The nozzle wall was covered with a 0.14 mm tape, sprayed with a high-emissivity graphite paint (DGF - Dry Graphite Film Spray) with a measured emissivity of  $0.90 \pm 0.02$ . The probe stems were sprayed directly with the same paint to ensure emissivity matching.

For each test condition (heated and unheated), two independent in-situ calibrations were conducted. The uncalibrated infrared temperature measured on the graphite-coated tape over the nozzle wall was compared to the corresponding thermocouple reading. For temperature variations within 200 K, the IR response can be assumed linear, allowing a linear fit to be applied to extract calibration coefficients and their associated uncertainties (Figure 7a). These coefficients were then used to retrieve the temperature in the stem of the probe.

At each setpoint, the stem temperature was evaluated by averaging the IR data over a 10-seconds window within a 15×15 pixel region centered around the sensor. The temporal variation of this spatial average is presented in Figure 7b, along with the  $\pm 2\sigma$  bounds of the resulting normal distribution. This indicates a temperature non-uniformity of approximately 2 K across the region of interest.

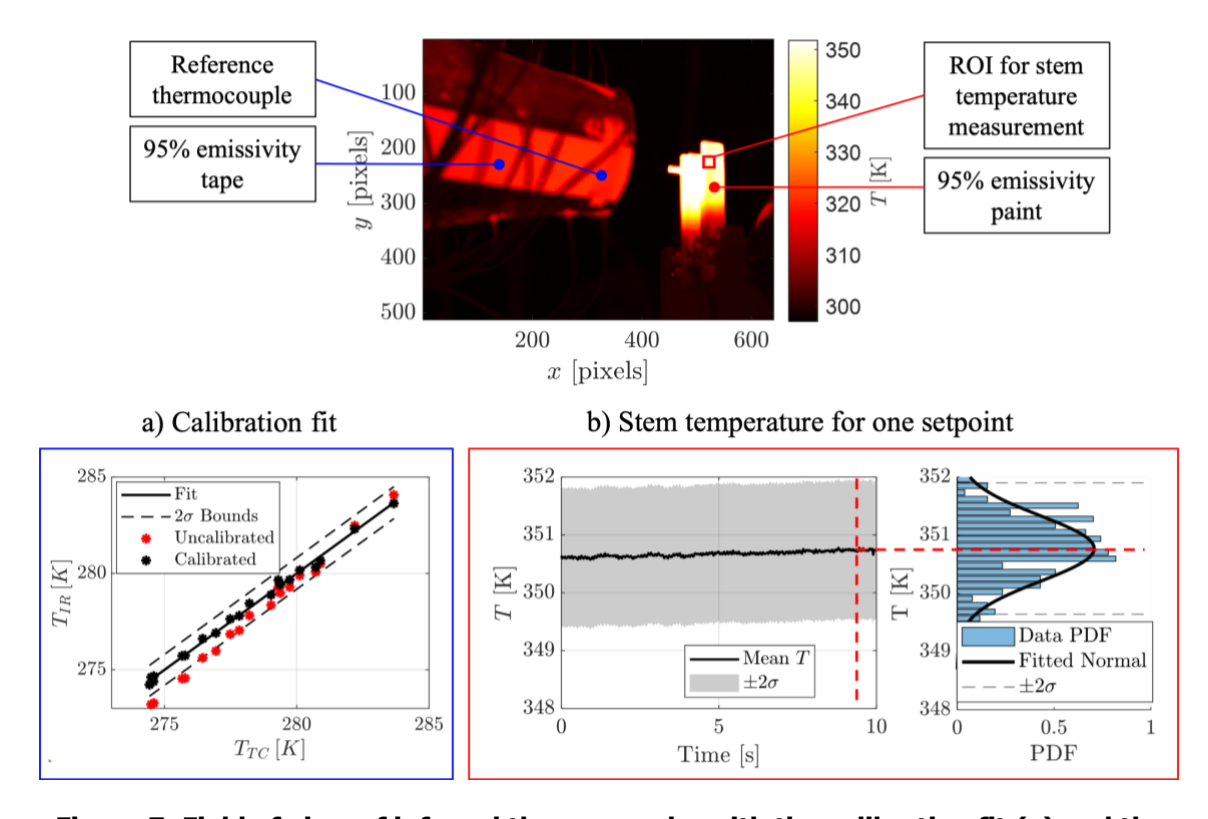


Figure 7. Field of view of infrared thermography with the calibration fit (a) and the spatial and temporal variation of temperature in the ROI in the stem for a given setpoint.

For the Infrared measurements, the bias uncertainty of the fit coefficients that convert from uncalibrated  $R_{IR}$  to calibrated  $T_{IR}$  and the bias uncertainty of the sensor of the IR camera are combined with the stochastic uncertainty of the IR signal to give values of the total uncertainty at each setpoint. In the formulas, the sensor bias  $B_{R_{IR}}$  is set to the Noise-Equivalent Temperature Difference of the TELOPS Fast V1K, which is 30 mK. The fit function for the IR correction is shown in Equation 27 and the bias and stochastic uncertainties during the test are measured using Equation 28.

$$T_{IR} = c_0 R_{IR} + c_1 (27)$$

$$B_{IR} = \sqrt{\left(R_{IR}B_{c_0}\right)^2 + \left(B_{c_1}\right)^2 + \left(c_0B_{R_{IR}}\right)^2}, \qquad \sigma_{IR} = \sqrt{\left(c_0\frac{S_{R_{IR}}}{\sqrt{N-1}}\right)^2}$$
 (28)

#### 4.2.3. Uncertainty in Velocity and Conduction Error Calibration

For the temperature and pressure readings, the bias uncertainty of the calibration coefficients comes from the static calibration, the stochastic uncertainty comes from the noise in the test data, and combined they give new values of the total uncertainty during the test.

With the uncertainties of the sensor temperature, total temperature, and stem temperature established, the remaining inputs required for the fit function are the uncertainties in Mach and Reynolds numbers. The Mach number is determined from the isentropic pressure ratio, so its uncertainty is obtained by propagating the uncertainties in total and static pressure through the Mach number formula. The uncertainty in the Reynolds number, in turn, depends on those of velocity, dynamic viscosity, and density. Knowing the Mach number and total temperature with their respective uncertainties allows the computation of static temperature, followed by dynamic viscosity (via Sutherland's law), velocity, and density, each with their propagated uncertainties using Taylor expansion.

Once all the input variables to the fit, along with their associated uncertainties, are known, a Monte Carlo approach with random sampling is employed to account for the uncertainty in both the input variables and nonlinear fit coefficients and estimate the combined uncertainty in the output (corrected sensor temperature) [36]. This method provides a more practical and robust alternative to analytical uncertainty propagation using Taylor series, particularly for nonlinear models. One million iterations of the fit function are performed, with each input parameter randomly perturbed within its uncertainty bounds. This generates one million sets of fit coefficients and corresponding output values. A normal distribution is then fitted to these results to estimate the standard deviation, representing the propagated uncertainty in the final output.

## 5. Temperature Errors in thermocouples and FBG probes

#### 5.1. Assessment of the use of the fit function

This section presents the results of fitting the experimental data to the functional form introduced in Section 2. Figures 8a and 8b illustrate the difference between the true total temperature and the sensor temperature before and after applying the correction. For the thermocouple, the maximum overall error in the uncorrected case reaches 1.5 K during the heated test at Mach 1.1, while the corrected case reduces the maximum error to below 0.25 K. In contrast, the FBG probe exhibits larger errors: the maximum uncorrected error of 5 K is reduced to approximately 1 K after correction.

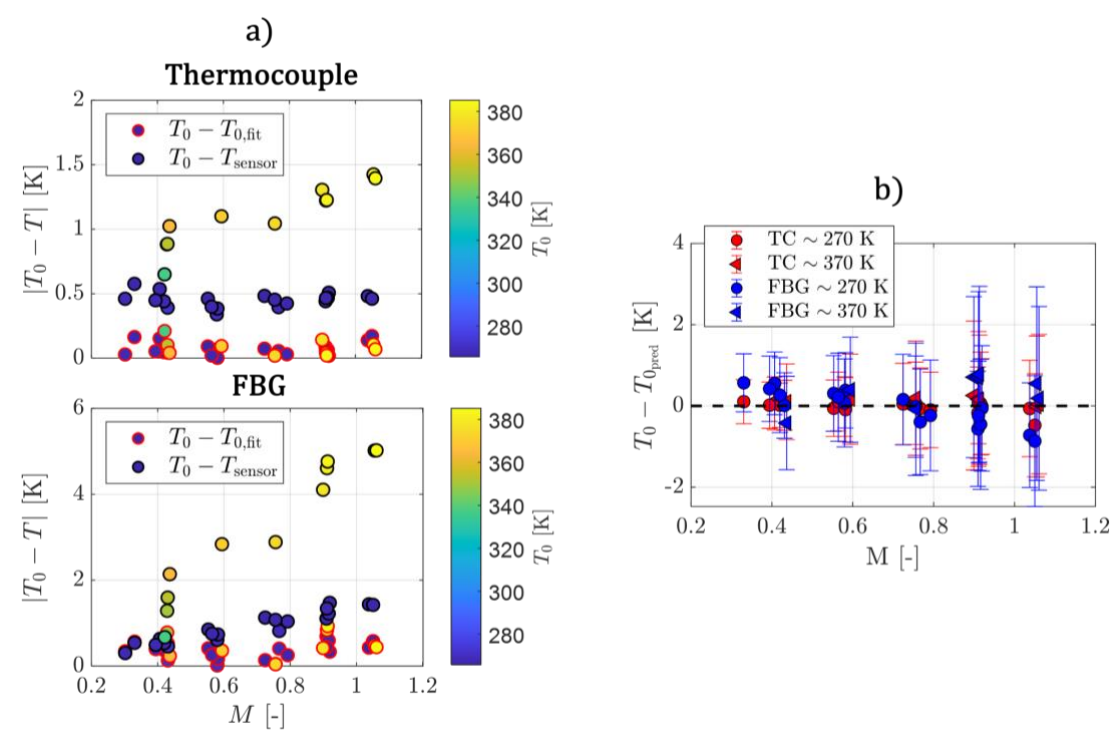


Figure 8. Difference between total temperature and sensor temperature with and without correction for thermocouple (a) and FBG (b), with the associated uncertainty bands (c).

Page | 13

The larger discrepancies observed for the FBG are likely due to effects that are unique for fiber-based sensors, such as the use of protective coatings around the grating to restrict strain. In the specific FBG probe used, the grating is not in direct contact with the flow stream; it is encased in PEEK, which increases the time required to reach thermal equilibrium, and adds another resistive element between the flow temperature and the sensor.

Figure 8c presents the corrected temperature differences for both probes, including the uncertainty bands propagated through the fit using the Monte Carlo scheme. These results highlight the necessity of coupling probe design with correction methodologies. Well-designed probes minimize the need for extensive corrections, thereby limiting the associated increase in uncertainty. For the conventional probes tested here, the propagated 2 $\sigma$  uncertainty band after correction ranges from ±0.4 K at the lowest Mach number to ±1.8 K at the highest for the thermocouple, and from ±0.8 K to ±3 K for the FBG. Because conventional probes were intentionally selected to clearly demonstrate temperature errors, the required corrections—and the resulting uncertainties—are comparatively large.

## 5.2. Splitting into velocity and conduction error

Conventional approaches, such as treating the error contributions independently, replace all adiabatic temperatures with the sensor temperature in Equations (2) and (3), yielding recovery and dimensionless conduction factors as shown in Figure 9. The recovery factor exhibits the expected trend, but the lack of overlap among the two curves for the same sensor indicates additional non-geometric effects beyond velocity error. The conduction factor plot is also inconsistent: it should remain positive and decay toward zero with increasing Mach number, which is not observed, particularly in the unheated test. These discrepancies demonstrate that, in high-temperature, high-speed flows with conventional probes, conduction and velocity errors are strongly coupled.

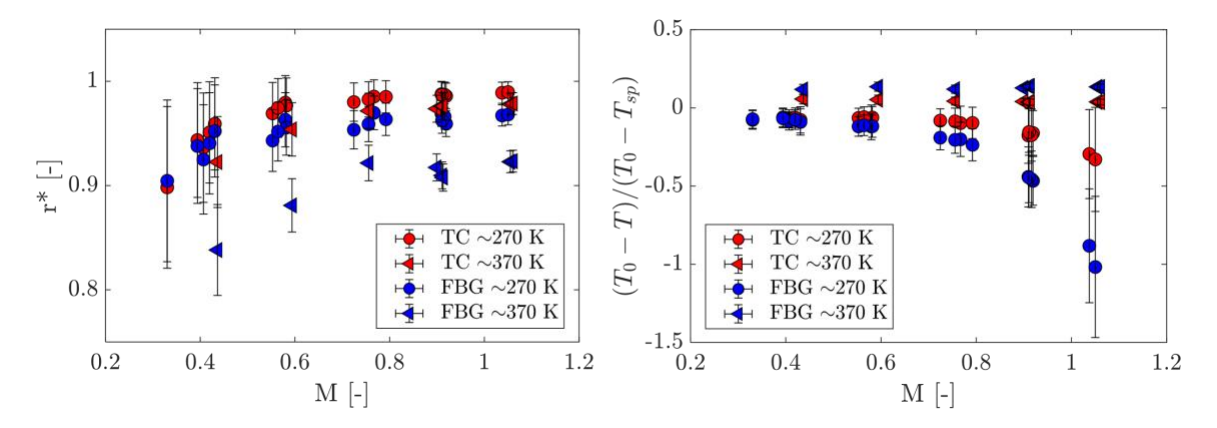


Figure 9. Pseudo-recovery factor and Pseudo-dimensionless conduction error if the independent effects assumption is used.

After applying the correction, the recovery factor and dimensionless conduction error for both the thermocouple and FBG are shown in Figure 10. The overall trends agree with previous observations by Sanchez and Paniagua [29], and Moffat [24].

The recovery factors of both probes stabilize at high values due to their shielding, reaching maxima of 0.98 for the thermocouple and 0.95 for the FBG at Mach numbers above 0.8. The results for the two probes are very similar and, in most cases, fall within the uncertainty bands of one another, consistent with the recovery factor being primarily a function of probe geometry, which is identical for both casings. The small differences are likely due to the sensing location in the FBG not being directly exposed to the flow; instead, the stagnation point is experienced by the PEEK enclosure, which subsequently transfers heat to the internal grating.

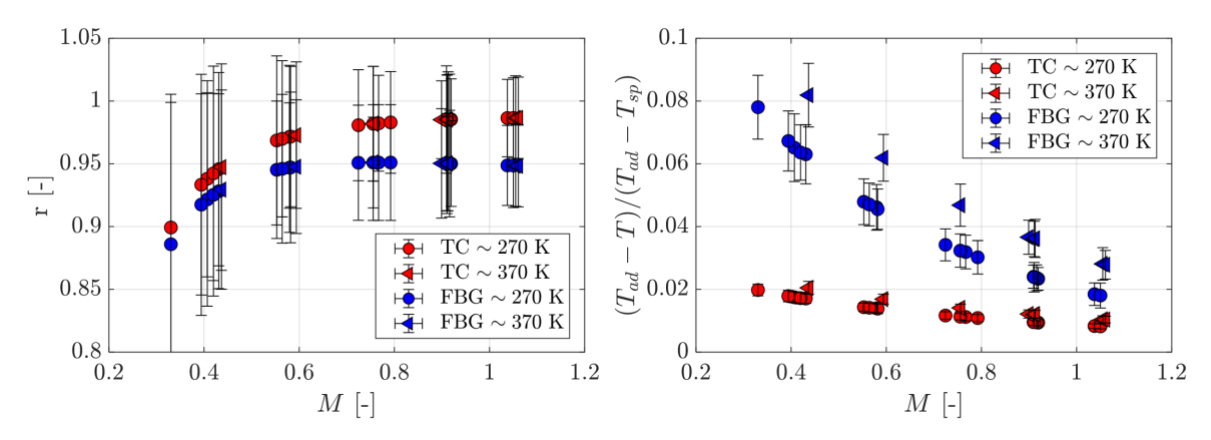


Figure 10. Recovery factor and dimensionless conduction error after splitting the error contributions into velocity and conduction based

The dimensionless conduction factor increases at low Mach numbers, where the Nusselt number is small, and conduction dominates heat transfer. The error in this regime is noticeably larger for the FBG. In theory, conduction errors should be reduced in the FBG, as its PEEK casing has very low thermal conductivity. A low-conductivity material is generally advantageous because it limits heat transfer to the casing, bringing the sensor reading closer to the flow temperature. However, since the FBG is not in direct contact with the flow, the low thermal conductivity of the PEEK enclosure also impedes rapid heat transfer from its outer surface to the internal grating—a limitation that is most pronounced at low Mach numbers. In this regime, the uncertainty bands of the two probes no longer overlap, confirming that conduction error is significantly different between them.

Figure 11 presents the relative contribution of conduction error to the total measurement error as a function of Mach number for both probes. This representation was used by Villafañe and Paniagua to compare different thermocouple probes, and it ranges from 0 (error entirely due to velocity effects) to 1 (error entirely due to conduction effects). [25]. At low Mach numbers, conduction dominates in both cases, but its relative importance is significantly higher for the FBG, reaching up to 80%, likely due to the insulating effect of the PEEK enclosure that amplifies the temperature difference between the flow and the sensor. Flow heating does not alter these low-Mach trends, as the relative contributions overlap for heated and unheated tests. At higher Mach numbers, the conduction contribution decreases below 30% for both probes, with heated flow tests showing higher values due to the increased temperature gradient between the flow and the stem. In this regime, both probes exhibit similar behavior, suggesting that the elevated Nusselt numbers enhance heat transfer through the FBG's PEEK enclosure, leaving conduction to the probe stem as the only conduction effect remaining for both probes.

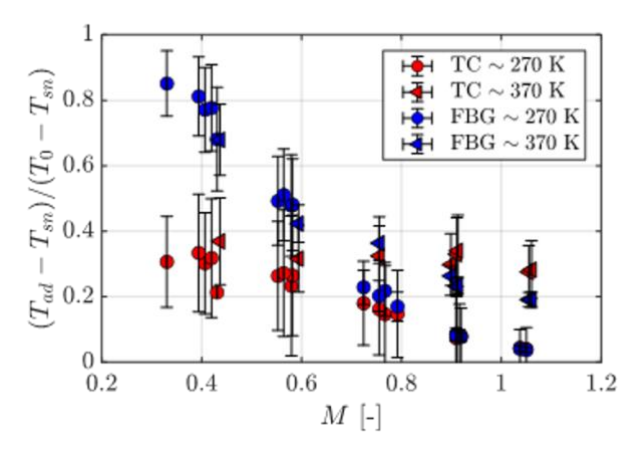


Figure 11. Relative contribution of conduction error with respect to the total temperature error for both probes.

#### 6. Conclusions

This work has presented an analytical framework to quantify and correct velocity- and conduction-related errors in total temperature measurements relying only on experimental measurements. Apart from thermocouples, this framework has been applied to off-the-shelf Fiber Bragg Grating sensors to characterize and compare the sensitivity of each probe to both temperature errors. The framework eliminates the dependence on difficult-to-access quantities in experimental facilities such as the internal casing temperature by reformulating the conduction model in terms of the external casing temperature. The adiabatic wall temperature is also made implicit in the formulation so that it does not have to be directly measured, as measuring in truly adiabatic condition is not realistic. The resulting functional form, calibrated experimentally, enables direct recovery of the true stagnation temperature with quantifiable uncertainties from Monte-Carlo propagation.

Application of the methodology in the FIOR facility across a wide range of Mach numbers and heating conditions demonstrated that temperature errors in conventional probes can reach up to 1.5 K for thermocouples and 5 K for FBGs in a transonic flow (Mach 1.1) at moderate total temperatures (370 K). After correction, these errors were reduced to below 0.25 K and 1 K, respectively. The recovery factor and dimensionless conduction error trends agree with classical correlations, confirming the validity of the approach. While both probes exhibited similar recovery factors consistent with their identical stem geometries, the FBG showed significantly higher conduction error contributions at low Mach numbers, reaching up to 80% of the total error. This effect is attributed to its PEEK enclosure, which limited heat transfer to the stem (beneficial for reducing conduction error) but also hindered fast heat transfer to the enclosed grating (detrimental for reducing conduction error), and this last effect appeared to be dominant at low velocities. At higher Mach numbers, conduction contributions dropped below 30% for both probes, indicating that velocity effects became dominant. Additionally, the relative contributions collapsed for both probes, showing that the effect of the PEEK enclosure on hindering fast heat transfer reduced at higher Nusselt numbers, and the conduction error for both probes became more similar.

Overall, the developed formulation provides a generalized and experimentally implementable correction strategy that is extendable to different probe types beyond thermocouples and FBGs. These insights pave the way for more accurate and transferable total temperature measurements in high-speed, high-temperature flows, with direct applicability to aerospace testing and diagnostics.

#### 7. References

- [1] D. R. Buttsworth and T. V. Jones, "A Fast-Response Total Temperature Probe For Unsteady Compressible Flows," *J Eng Gas Turbine Power*, vol. 120, no. 4, pp. 694–702, Oct. 1998, doi: 10.1115/1.2818456.
- [2] D. L. Goldstein and R. Scherrer, "Design and Calibration of a Total-Temperature Probe for Use at Supersonic Speeds, NACA TN 1885," 1949.
- [3] J. Reardon, J. A. Schetz, and K. T. Lowe, "Computational Modeling of Total-Temperature Probes," *J Thermophys Heat Trans*, vol. 31, no. 3, pp. 609–620, Jul. 2017, doi: 10.2514/1.T4991.
- [4] D. Sánchez de la Rosa and G. Paniagua, "Enhancing Total Temperature Measurement Accuracy: Calibration Procedures and Novel Two-Wire Probes," *J Turbomach*, vol. 147, no. 5, May 2025, doi: 10.1115/1.4066964.
- [5] K. O. Hill and G. Meltz, "Fiber Bragg Grating Technology Fundamentals and Overview," *Journal of Lightwave Technology*, vol. 15, no. 8, pp. 1263–1276, 1997, doi: 10.1109/50.618320.
- [6] A. D. Kersey, "A Review of Recent Developments in Fiber Optic Sensor Technology," *Optical Fiber Technology*, vol. 2, no. 3, pp. 291–317, Jul. 1996, doi: 10.1006/ofte.1996.0036.
- [7] C. V. N. Bhaskar, S. Pal, and P. K. Pattnaik, "Recent advancements in fiber Bragg gratings based temperature and strain measurement," *Results in Optics*, vol. 5, p. 100130, Dec. 2021, doi: 10.1016/j.rio.2021.100130.
- [8] L. Polz, F. J. Dutz, R. R. J. Maier, H. Bartelt, and J. Roths, "Regenerated Fibre Bragg Gratings: A critical assessment of more than 20 years of investigations," *Opt Laser Technol*, vol. 134, p. 106650, Feb. 2021, doi: 10.1016/j.optlastec.2020.106650.

- [9] S. J. Mihailov, "Fiber Bragg Grating Sensors for Harsh Environments," Sensors, vol. 12, no. 2, pp. 1898-1918, Feb. 2012, doi: 10.3390/s120201898.
- T. Habisreuther, T. Elsmann, Z. Pan, A. Graf, R. Willsch, and M. A. Schmidt, "Sapphire fiber [10] Bragg gratings for high temperature and dynamic temperature diagnostics," Appl Therm Eng, vol. 91, pp. 860–865, Dec. 2015, doi: 10.1016/j.applthermaleng.2015.08.096.
- [11] Q. Bian et al., "Characterization of High-Temperature Performance of a Sapphire Fiber Bragg Grating With a Single-Mode Demodulation System," IEEE Sens J, vol. 24, no. 7, pp. 10138-10143, Apr. 2024, doi: 10.1109/JSEN.2024.3366230.
- [12] R. B. Walker et al., "High temperature measurement of a low emission, high pressure combustor using femtosecond laser written fiber Bragg gratings," in Fiber Optic Sensors and Applications XV, H. H. Du, A. Mendez, and C. S. Baldwin, Eds., SPIE, May 2018, p. 7. doi: 10.1117/12.2304489.
- R. B. Walker et al., "High-resolution fast temperature mapping of a gas turbine combustor [13] simulator with femtosecond infrared laser written fiber Bragg gratings," in Photonic Instrumentation Engineering IV, Y. G. Soskind and C. Olson, Eds., SPIE, Feb. 2017, p. 101101H. doi: 10.1117/12.2251037.
- J. Roths et al., "Multipoint high temperature sensing with regenerated fiber Bragg gratings," in [14] Fiber Optic Sensors and Applications XV, H. H. Du, A. Mendez, and C. S. Baldwin, Eds., SPIE, May 2018, p. 6. doi: 10.1117/12.2305300.
- S. Spolitis, I. Lyashuk, and V. Bobrovs, "Design and performance evaluation of FBG-based [15] temperature sensors network," in 2017 Progress in Electromagnetics Research Symposium - Fall (PIERS - FALL), Singapore: IEEE, Nov. 2017, pp. 2673-2678. doi: 10.1109/PIERS-FALL.2017.8293590.
- F. Buchfellner et al., "Generalized and wavelength-dependent temperature calibration function for multipoint regenerated fiber Bragg grating sensors," Opt Express, vol. 30, no. 25, p. 44769, Dec. 2022, doi: 10.1364/OE.470093.
- F. J. Dutz, S. Boje, U. Orth, A. W. Koch, and J. Roths, "High-Temperature Profile Monitoring in [17] Gas Turbine Exhaust-Gas Diffusors with Six-Point Fiber-Optic Sensor Array," International Journal of Turbomachinery, Propulsion and Power, vol. 5, no. 4, p. 25, Sep. 2020, doi: 10.3390/ijtpp5040025.
- A. Stadler, A. Zeisberger, F. Buchfellner, A. Roehrl, A. W. Koch, and J. Roths, "Accurate high-[18] temperature profile sensing with dense multipoint arrays of regenerated fiber Bragg gratings," Results Phys, vol. 65, p. 107970, Oct. 2024, doi: 10.1016/j.rinp.2024.107970.
- J. Liu et al., "Fiber Bragg Grating-based sensor for measuring supersonic inlet terminal shock at [19] different angles of attack," Measurement, vol. 242, p. 115985, Jan. 2025, doi: 10.1016/j.measurement.2024.115985.
- [20] L. Pollock, H. Kleine, A. Neely, and G. Wild, "Optical Fiber Bragg Grating-Based Measurement of Fluid-Structure Interaction on a Cantilever Panel in High-Speed Flow," *IEEE Access*, vol. 12, pp. 101106-101120, 2024, doi: 10.1109/ACCESS.2024.3430219.
- Society of Automotive Engineers, "Thermoelectric Circuits and the Performance of Several Jet Engine Thermocouples. SAE Aeronautical Information Report A.I.B-65," 1956.
- [22] Society of Automotive Engineers, "Preparation and Use of Chromel-Alumel Thermocouples for Turbo-Jet Engines. SAE Aeronautical Information Report A.I.R-46," 1958.
- [23] E. M. Moffatt, "Errors in High Temperature Probes for Gases," ASME Preprint, no. 48-A, p. 52, 1948.
- R. J. Moffat, "Gas Temperature Measurement," in Temperature: Its Measurement and Control [24] in Science and Industry, vol. 3, 1962, ch. 52, pp. 553–571.
- L. Villafañe and G. Paniagua, "Aero-thermal analysis of shielded fine wire thermocouple probes," [25] International Journal of Thermal Sciences, vol. 65, pp. 214–223, 2013.
- F. P. Incropera, D. P. DeWitt, T. L. Bergman, and A. S. Lavine, Fundamentals of heat and mass [26] transfer, vol. 6. Wiley New York, 1996.
- R. D. Wood, "An experimental investigation of hypersonic stagnation temperature probes," [27] California Institute of Technology, 1959.
- R. F. Nares Alcala, L. Bhatnagar, and G. Paniagua, "Development of a conduction-free total [28] temperature probe based on the two-wire thermocouple concept," in Turbo Expo: Power for Land, Sea, and Air, American Society of Mechanical Engineers, 2023, p. V004T05A016.

- [29] D. Sanchez De La Rosa and G. Paniagua, "Enhancing Total Temperature Measurement Accuracy: Calibration Procedures and Novel Two-Wire Probes," *J Turbomach*, vol. 147, no. 5, p. 051006, 2025.
- [30] M. D. Scadron and I. Warshasky, "Experimental determination of time constants and Nusselt numbers for bare-wire thermocouples in high-velocity air streams and analytic approximation of conduction and radiation errors," 1952.
- [31] G. Paniagua *et al.*, "Design of the Purdue experimental turbine aerothermal laboratory for optical and surface aerothermal measurements," *J Eng Gas Turbine Power*, vol. 141, no. 1, p. 012601, 2019.
- [32] H. I. Saravanamuttoo, "Recommended Practices for Measurement of Gas Path Pressures and Temperatures for Performance Assessment of Aircraft Turbine Engines and Components (Les Methodes Recommandees pour la Mesure de la Pression et de la Temperature de la Veine Gazeuse en Vue de l'Evaluation des Performances des Turbines Aeronautiques et de leurs Composants," 1990.
- [33] G. W. Burns, *The calibration of thermocouples and thermocouple materials*, vol. 250, no. 35. US Department of Commerce, National Institute of Standards and Technology, 1989.
- [34] VDI/VDE, "Technical temperature measurement Optical temperature sensor based on fibre Bragg gratings Recommendation on temperature measurement and statement of measurement uncertainty. VDI/VDE 2660 Blatt 2," 2020.
- [35] T. Ostrowski and H. P. Schiffer, "High-resolution heat transfer measurements on a rotating turbine endwall with infrared thermography," *Meas Sci Technol*, vol. 32, no. 12, p. 125207, 2021.
- [36] M. J. W. Jansen, W. A. H. Rossing, and R. A. Daamen, "Monte Carlo estimation of uncertainty contributions from several independent multivariate sources," in *Predictability and nonlinear modelling in natural sciences and economics*, Springer, 1994, pp. 334–343.